Edge-induced excitations in Bi_2Te_3 from spatially-resolved electron energy-gain spectroscopy

La, Helena; Brokkelkamp, Abel; van der Lippe, Stijn; ter Hoeve, Jaco; Rojo, Juan; Conesa-Boj, Sonia

Important note
To cite this publication, please use the final published version (if applicable).
Please check the document version above.

Edge-induced excitations in Bi_2Te_3 from spatially-resolved electron energy-gain spectroscopy

Helena La [a,1], Abel Brokkelkamp [a,1], Stijn van der Lippe [a,1], Jaco ter Hoeve [b,c], Juan Rojo [b,c], Sonia Conesa-Boj [a,*]

[a] *Kavli Institute of Nanoscience, Delft University of Technology, Delft, 2628 CJ, The Netherlands*
[b] *Nikhef Theory Group, Science Park 105, 1098 XG Amsterdam, The Netherlands*
[c] *Department of Physics and Astronomy, VU, 1081 HV Amsterdam, The Netherlands*

ARTICLE INFO

ABSTRACT

Among the many potential applications of topological insulator materials, their broad potential for the development of novel tunable plasmonics at THz and mid-infrared frequencies for quantum computing, terahertz detectors, and spintronic devices is particularly attractive. The required understanding of the intricate relationship between nanoscale crystal structure and the properties of the resulting plasmonic resonances remains, however, elusive for these materials. Specifically, edge- and surface-induced plasmonic resonances, and other collective excitations, are often buried beneath the continuum of electronic transitions, making it difficult to isolate and interpret these signals using techniques such as electron energy-loss spectroscopy (EELS). Here we focus on the experimentally clean energy-gain EELS region to characterise collective excitations in the topologically insulating material Bi_2Te_3 and correlate them with the underlying crystalline structure with nanoscale resolution. We identify with high significance the presence of a distinct energy-gain peak around −0.8 eV, with spatially-resolved maps revealing that its intensity is markedly enhanced at the edge regions of the specimen. Our findings illustrate the reach of energy-gain EELS analyses to accurately map collective excitations in quantum materials, a key asset in the quest towards new tunable plasmonic devices.

1. Introduction

Topological insulator (TI) materials, such as Bi_2Te_3 [1–3] and Bi_2Se_3, possess unique properties that make them well suited for the design of nanoplasmonic devices operating in the THz and mid-infrared frequency ranges [4–8]. Topological insulators can also support plasmonic excitations, collective oscillations of electrons that interact strongly with light or other electrons and lead to enhanced light-matter interactions such as strong scattering, absorption, and emission. In particular, low-energy plasmons [9] have been reported in Bi_2Te_3 below 3 eV while correlated plasmons at energies ∼1 eV have been identified for Bi_2Se_3 [10]. In this context, advancing our understanding of how to optimally deploy TIs for the development of tunable plasmonic devices that operate efficiently in optical frequencies has the potential to benefit a wide range of applications, including quantum computing [11,12], terahertz detectors [13], and spintronic devices [14].

In recent years, significant progress has been achieved in resolving plasmon resonances at the nanoscale, providing valuable information about the spatial and spectral distribution of plasmonic modes.

To this end, electron-based spectroscopic techniques such as electron energy-loss spectroscopy (EELS) have demonstrated their suitability to investigate the electronic and optical properties of a wide range of materials, including the study of their plasmonic resonances [15–21]. In parallel, advances in transmission electron microscopy (TEM) have resulted in novel opportunities for scrutinising the functionalities of nanostructured materials. For instance, the incorporation of monochromators and aberration correctors makes it possible to resolve collective lattice oscillations (phonons) and study them with nanometer spatial resolution [22–27]. Furthermore, the incorporation of machine learning (ML) algorithms for EELS data analysis and interpretation has further enhanced the reach of spectroscopic techniques to pin down the properties of nanomaterials. As recently demonstrated [28,29], ML methods enable the spatially-resolved determination of local electronic properties such as the band gap and the dielectric function with nanometer resolution from EELS spectral images

Here we investigate low-energy collective excitations in the TI material Bi_2Te_3 by means of EELS spectral images focusing on the

---

* Corresponding author.
E-mail address: s.conesaboj@tudelft.nl (S. Conesa-Boj).
[1] Equal contribution.

energy-gain ($\Delta E < 0$) region [20,30–32]. As compared to traditional EELS, this strategy offers the key advantage that gain peaks are not obscured by the multiple scatterings continuum and other electronic transitions taking place in the energy-loss region ($\Delta E > 0$), enabling the clean identification of narrow collective excitations with enhanced spectral resolution. The resulting characterisation of Bi_2Te_3 specimens makes it possible to search for collective resonances in the low-gain region, and correlate their spatial distribution with distinct structural features such as surfaces, edges, and regions with sharp thickness variations.

Our analysis reveals the presence of a narrow energy-gain peak around -0.8 eV whose intensity is the largest in regions of the specimen associated with exposed edges and surfaces. We demonstrate the robustness of our energy-gain peak identification algorithm with respect to the strategy adopted for the modelling and subtraction of the dominant zero-loss peak (ZLP) background, quantify the statistical significance of this signal, and estimate procedural uncertainties by means of the Monte Carlo method widely used in high-energy physics. Our work represents a significant step forward in exploiting the information contained in the energy-gain region of EELS spectral images to achieve an improved understanding of localised collective resonances in TI materials.

2. Results and discussion

Fig. 1a displays a high-angle annular dark-field (HAADF) Scanning Transmission Electron Microscopy (STEM) image of a representative Bi_2Te_3 specimen. For closer examination, Fig. 1b shows the magnified top right corner of the same specimen. Further characterisation of the atomic structure of this specimen is provided in SI-S1 of the Supplementary Material. By means of electron energy-loss spectroscopy (EELS), we acquire a spectral image (Fig. 1c) of the specimen in the same region, indicated with a white square in Fig. 1a. The colour map corresponds to the integrated intensity in the energy range $[-9.05, 92.3]$ eV in each pixel, covering the total energy range in which signal was acquired. The black line indicates the edge of the Bi_2Te_3 specimen, which is automatically determined from the spatially-resolved thickness map associated to the spectral image [28], specifically from its local rate of change.

Fig. 1d displays EELS spectra taken at three different locations within the spectral image, labelled as spectra sp1, sp2, and sp3 in the following. Spectra sp1, sp2, and sp3 are acquired in the region between the vacuum and the edge of the specimen, in the vicinity of the specimen edge towards the inner region, and in the innermost part of the specimen, respectively. The three spectra reveal the presence of distinct spectral features located at approximately energy losses of 8.6 eV and 16.6 eV, where the latter corresponds to the bulk plasmon peak in accordance with previous studies [33]. Furthermore, the peaks at 25.6 eV and 27.9 eV observed in sp3 can be identified with the Bi $O_{4,5}$ edges excited from Bi $5d$ electrons, also reported in the literature [34]. Fig. 1e compares three other EEL spectra (labelled as sp4, sp5, and sp6) acquired in the immediate vicinity of the specimen edge. The three spectra exhibit a broad peak located around 21 eV, which can be identified with the bulk plasmon of Bi_2O_3 [35,36]. It is worth nothing that the presence of Bi_2O_3 in the surfaces of the specimen is not visible from the HAADF images. The reason is that HAADF intensity scales with Z^n, with Z being the atomic number, which is much smaller in O as compared to Te. This presence of Bi_2O_3 in the edge region of the Bi_2Te_3 specimen is further supported by a High-Resolution TEM (HRTEM) analysis reported in SI-S6 of the Supplementary Material.

Fig. 1f compares the EELS intensities in the region of energy losses ΔE restricted to the window $[-2 \text{ eV}, 2 \text{ eV}]$ for spectra sp2, sp3, and sp7. This comparison illustrates the dependence of the dominant Zero-Loss Peak (ZLP) background with respect to the location in the specimen: bulk (sp3), close to edge (sp2), and vacuum (sp7). On the one hand, as one moves from the vacuum towards the bulk region, the ZLP

intensity gradually decreases. This effect can be ascribed to the greater number of inelastic scattering events that occur in the bulk (thicker) regions, compared to the vacuum where the beam electrons do not experience inelastic scatterings. On the other hand, we also observe an enhanced intensity in the specimen regions as compared to the vacuum for $|\Delta E| \geq 0.6$ eV, highlighting material-sensitive contributions to the spectra which contain direct information on its local electronic properties.

Removing this ZLP background is instrumental in order to identify the presence of localised collective excitations such as phonons [24] and plasmon peaks [21] in the low energy-loss region. The same considerations apply to the cleaner energy-gain region [32], where the continuum of inelastic scattering contributions is absent. Here we model the ZLP in terms of a Gaussian distribution following the procedure described in SI-S2, with the fitting region restricted to $[-0.4, 0.4]$ eV to remove the overlap with ΔE values at which plasmonic modes of Bi_2Te_3 have been reported [9]. Subsequently, the ZLP is removed pixel by pixel in the EELS spectral image and the resulting spectra are inspected to identify peaks and other well-defined features in an automated manner. We note that the small band gap [3,14] of Bi_2Te_3, $E_{bg} \sim 0.15$ eV, prevents reliably training deep learning models for the ZLP parametrisation and subtraction as done in previous studies from our group [28,29,37]. Furthermore, although here we focus on a Bi_2Te_3 specimen, the procedure is fully general and applicable to other materials which can be inspected with EELS.

Fig. 2 summarises the adopted strategy for the spatially-resolved identification of energy-gain peaks. First, Fig. 2a shows the EEL spectrum for the pixel indicated with a star in Fig. 1c together with the corresponding ZLP fit. Closing up on the energy-gain region, Fig. 2b displays the resulting subtracted spectrum, to which a Lorentzian function is fitted (see SI-S2 for details) to extract the position E_g and intensity of the dominant energy-gain peak. The procedure is repeated for the complete EELS spectral image, making it possible to construct the spatially-resolved map of E_g shown in Fig. 2c across the inspected region of the Bi_2Te_3 specimen. As in Fig. 1c, the black line indicates the boundary of the Bi_2Te_3 sample. Fig. 2c reveals the presence of an energy-gain peak in the specimen with E_g values between -1.1 eV and -0.85 eV. We demonstrate in SI-S2 that results for the ZLP removal and energy-gain peak identification are robust with respect to the choice of ZLP model function. Then Fig. 2d displays the Bi_2Te_3 thickness map as obtained from the deconvolution of the single-scattering EELS distribution [28]. The dark blue region beyond the specimen corresponds to either the vacuum or the Bi_2O_3 regions. In the edge region there is a sharp increase in thickness, while in the bulk region the thickness exhibits an approximately constant value of 70 nm.

In order to further characterise the energy-gain peak identified in Fig. 2c and to correlate its properties with local structural features of the specimen, Fig. 3a and b display the intensity of the ZLP-subtracted EEL spectra integrated in the energy windows $[-1.1, -0.6]$ eV and $[0.6, 1.1]$ eV for the gain and loss regions respectively. These ΔE intervals are chosen to contain the range of E_g values displayed in Fig. 2c and then mirrored to the energy-loss region. In the latter case, the EEL spectra receive additional contributions to the inelastic scattering distribution beyond those considered here. The most notable feature of Fig. 3a is an enhancement of the integrated intensity in the edge region of the specimen characterised by a sharp variation of the local thickness (Fig. 2d).

To quantify the statistical significance of the identified energy-gain peak, it is convenient to evaluate the ratio

$$s_g \equiv \left(A_g / A_{zlp} \right)_{g-fwhm}, \tag{1}$$

where A_g and A_{zlp} are defined as the areas under the full width at half-maximum (FWMH) of the Lorentzian fit signal, filled region in Fig. 2b, and under the ZLP in the same ΔE region, respectively. In other words, s_g measures the significance of the energy-gain peak in units of the ZLP background. Fig. 3c displays a spatially-resolved map of s_g across
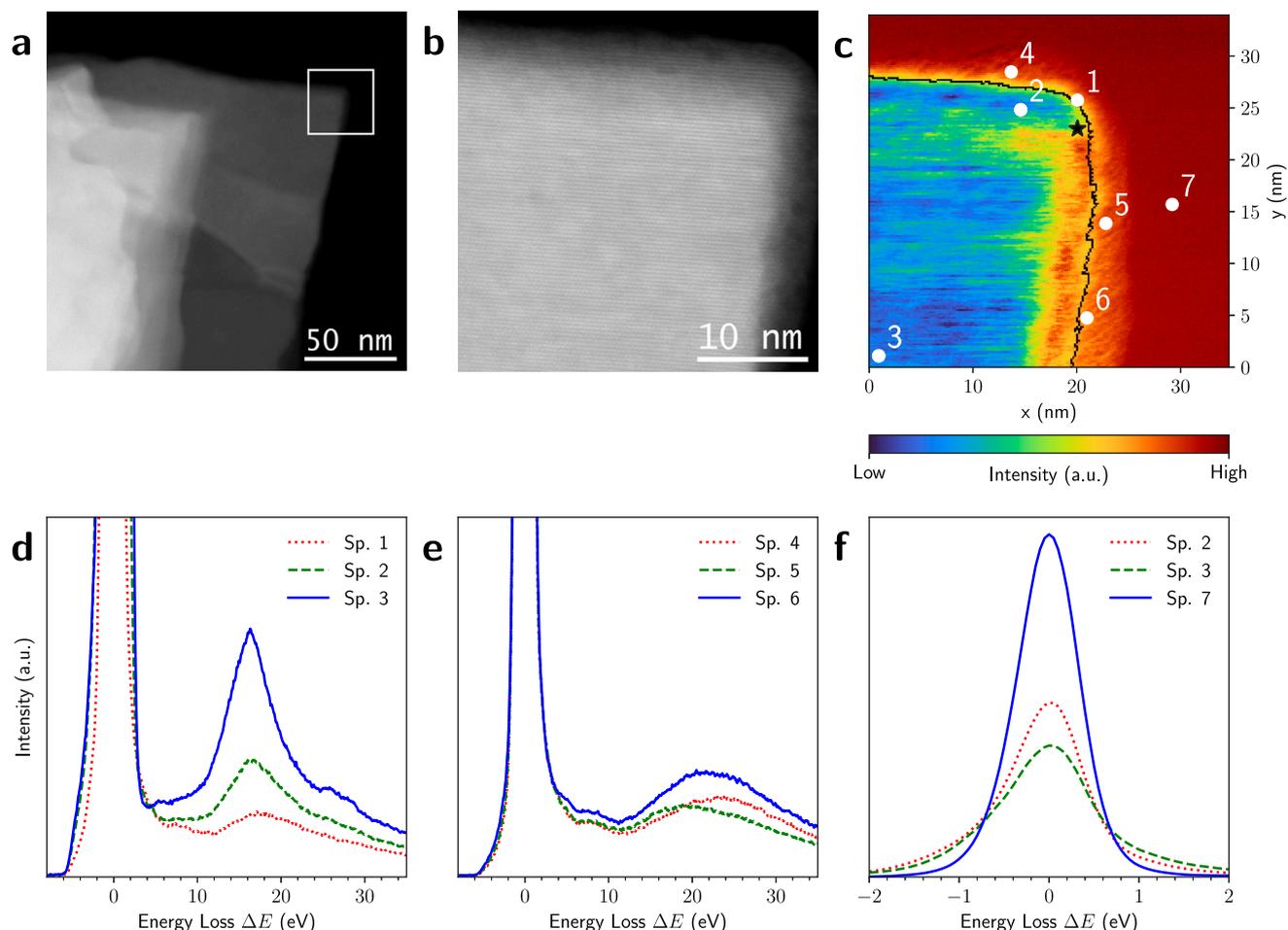
Fig. 1. Spatially-resolved EELS analysis of Bi_2Te_3. (a) HAADF-STEM image of a representative Bi_2Te_3 flake. (b) Magnified region of the top right corner of the specimen around the white square in (a). (c) EELS spectral image corresponding to the white square region in (a). The colour map corresponds to the total integrated intensity in each pixel. The black line indicates the edge of the Bi_2Te_3 specimen, determined from the thickness map as described in the text. (d) EELS spectra corresponding to the different regions of the specimen indicated in (c): between the vacuum and the edge (sp. 1); the vicinity of the edge towards the inner region (sp. 2); and the innermost, thicker part (sp. 3). Spectra sp. 1, sp. 2 and sp. 3 display the bulk plasmon peak of Bi_2Te_3 at around 16 eV. Additionally, sp. 3 also shows the Bi $O_{4,5}$ edges excited from Bi $5d$ electrons at 25.6 eV and 27.9 eV. (e) Same as (d) for EELS spectra in the immediate vicinity of the Bi_2Te_3 edge, displaying characteristic features of Bi_2O_3. (f) A comparison of sp. 2, sp. 3, and sp. 7 in the low loss and gain regions ($|\Delta E| \leq 2$ eV).

the specimen. The region of enhanced intensity reported in Fig. 3a and associated to the specimen edge corresponds to the highest values of s_g in Fig. 3c, reaching up to a factor two. This high significance confirms that the observe intensity enhancement in the gain region is a genuine feature of the data rather than an artefact of the ZLP removal procedure.

It is also interesting to compare the features of the approximately symmetric peaks appearing in the energy-gain and energy-loss regions, whose values E_g and E_ℓ respectively are mapped across the specimen in Fig. S3 of the Supplementary Material. One observes in general a stronger intensity of the energy-gain peak as compared to its energy-loss counterpart. To quantify this observation and to compare their relative intensities, we display in Fig. 3d the ratio A_g/A_ℓ of the areas under the FWHM of the energy-gain Lorentzian fit to that of the energy-loss peak. The vacuum region is masked out to facilitate readability. As can be seen, in the bulk of the sample the ratio A_g/A_ℓ is of the order unity, whereas in the edge region of the specimen the ratio reaches a factor of around 4. The latter result indicates that surface and edge effects enhance the relative intensity of the energy-gain peak. The combination Figs. 2 and 3 demonstrates the presence of a well-defined, significant energy-gain peak in Bi_2Te_3 located around $E_g \simeq -0.9$ eV whose intensity is enhanced in the edge regions of the specimen close to the boundary.

A potential limitation of this analysis concerns the lack of a systematic estimate of the functional uncertainties associated to the ZLP modelling and its subsequent subtraction from the EELS spectral image. To this purpose, we deploy the Monte Carlo replica method for error propagation, originally developed for proton structure studies in high-energy physics [38–42] and then extended to deep learning models of the ZLP within the EELSFITTER framework [28,29]. First, one applies K-means clustering to the EELS spectral image with the similarity measure being the area under the three bins of the EELS intensity around $\Delta E = 0$, which operates as a proxy for the local thickness map of Fig. 2d. This procedure results in the 20 clusters shown in Fig. 4a, each of them composed by pixels with similar thickness. Within each cluster, the EELS intensities are assumed to be sampled from the same underlying distribution, and N_{rep} spectra ("replicas") are randomly selected from each cluster. By fitting a separate ZLP model to each replica, one ends up with a sampling of N_{rep} models of the ZLP which can be used to estimate uncertainties and propagate them to the subtracted spectra and the subsequent Lorentzian fits.

Fig. 4b displays the same ZLP-subtracted spectrum as in Fig. 2b now with the Monte Carlo replica method used to estimate ZLP model uncertainties. For the ZLP fit, the subtracted spectrum, and the Lorentzian fit to the latter the bands indicate the 68% confidence level (CL) intervals evaluated over the N_{rep} replicas. By repeating this approach in all clusters, we calculate the area ratio s_g defined
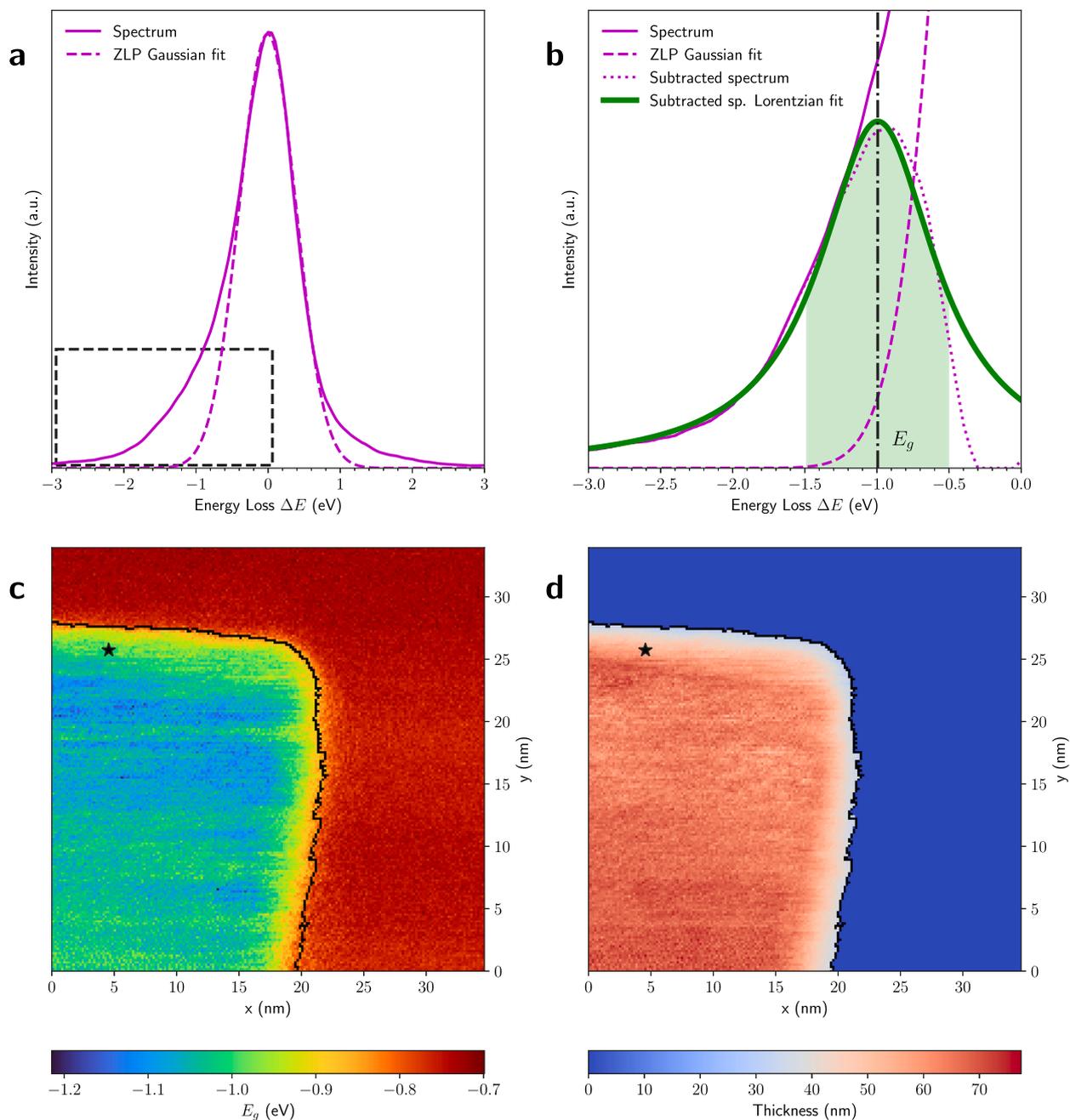
Fig. 2. Energy-gain peak identification in Bi$_2$Te$_3$. **(a)** The EEL spectrum (solid) in the pixel indicated with a star in Fig. 1**c** together with the corresponding fit to the ZLP (dashed curve). **(b)** Close-up of the dashed rectangle in **(a)**, now adding the Lorentzian fit (thick solid line) to the subtracted spectrum (dotted line). The vertical line indicates the mean of the Lorentzian energy-gain peak E_g, while the filled region indicates the corresponding FWHM. **(c)** Spatially-resolved map displaying the location of the energy-gain peak E_g, determined following the procedure of **(b)** across the whole spectral image of Fig. 1**c**. **(d)** Same as **(c)** now for the local specimen thickness. The dark blue region beyond the specimen edge corresponds to the vacuum region of the spectral image.

in Eq. (1) for all pixels in the spectral image using the replicas to propagate uncertainties. This results in lower and upper bounds of the 68% confidence interval of the area ratio shown in Fig. 4**c** and **d** respectively. The corresponding map of the median of s_g is consistent with that reported in Fig. 3**c** and shown in Fig. S4 in the Supplementary Material. Given that a good significance (above unity) of the energy-gain peak is still observed in the map of the lower limit of the 68% CL interval for the relevant edge region, one can conclude that the results of this work are not distorted by unaccounted-for methodological or procedural uncertainties.

To confirm the reproducibility of our findings, we have performed additional measurements on a different Bi$_2$Te$_3$ specimen characterised by the same crystal structure and with comparable features as the one discussed here. The resulting analysis is summarised in SI-S5 of the Supplementary Material and reveals the same qualitative features in the energy-gain region, namely a well-defined, narrow peak at energy gains around -0.7 eV whose intensity is enhanced in edge and surface regions and whose significance reaches values of $s_g \sim 4$. This independent analysis further confirms the robustness of our results, in particular the strong correlation between the enhanced intensity of the energy-gain
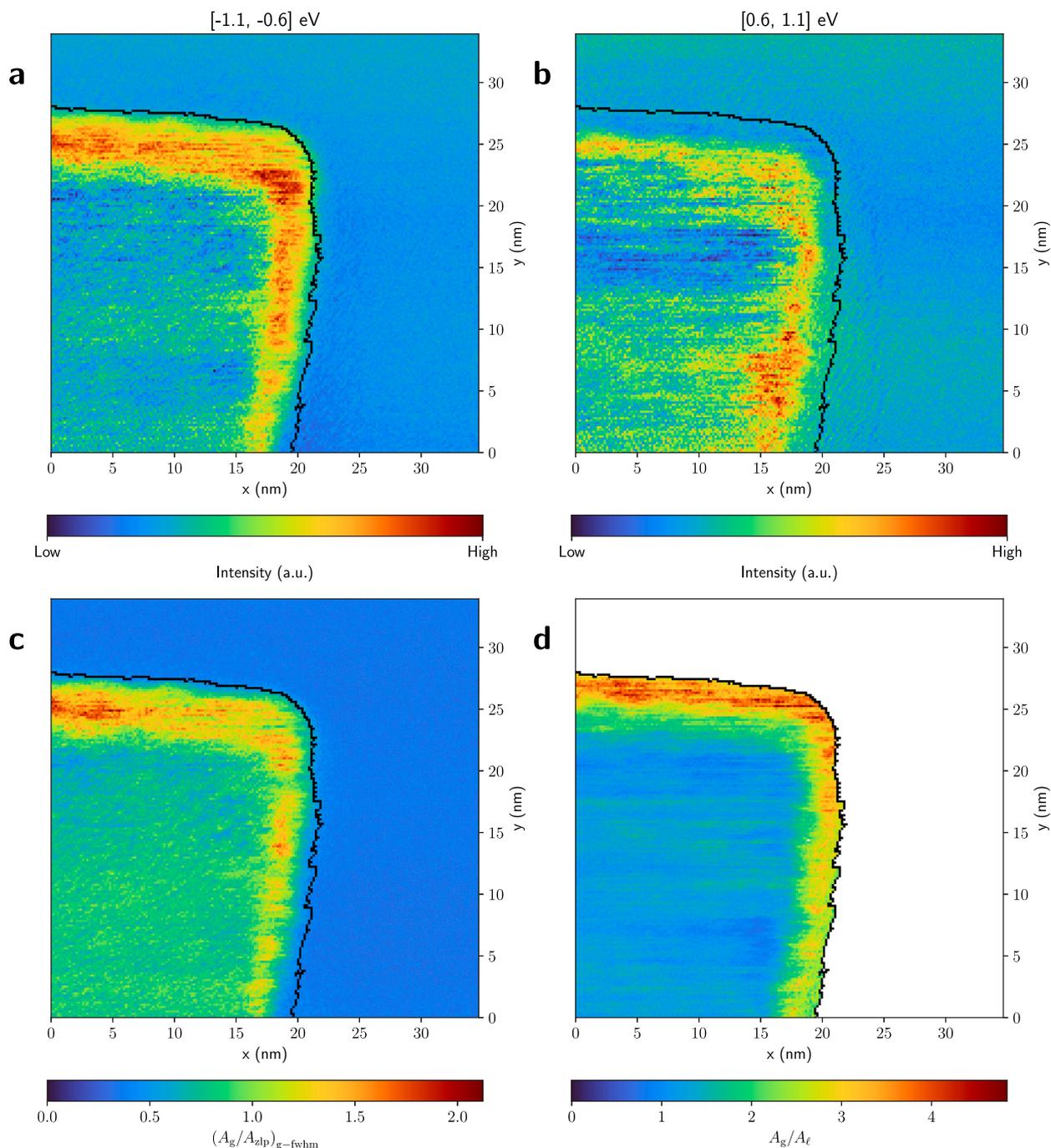
Fig. 3. Spatially-resolved characterisation of energy-gain peaks. **(a)** Same as Fig. 1**c**, now with the intensity of the EEL spectra (after ZLP subtraction) integrated in the window $[-1.1, -0.6]$ eV where the gain peak identified in Fig. 2**c** is located. **(b)** Same as **(a)** for the mirrored energy-loss window, $[0.6, 1.1]$ eV. **(c)** Spatially-resolved map of the ratio s_g, Eq. (1), defined as the area under the FWHM of the Lorentzian fit to the energy-gain peak, filled region in Fig. 2**b**, to the area under the ZLP in the same ΔE window. **(d)** Ratio of the area A_g under the FWHM of the Lorentzian fit to the energy-gain peak to its counterpart A_ℓ in the loss region, where the vacuum region is masked out for clarity.

peak located around $[-0.9, -0.7]$ eV and specimen regions displayed sharp thickness variations including edges and surfaces.

It is beyond our scope to identify the underlying physical phenomena leading to the observed edge- and surface-induced energy-gain peaks in Bi_2Te_3. Several mechanisms have been explored leading to resonance signatures in the ΔE region relevant for our results, such as wedge Dyakonov waves [43] and edge- and surface-located Dirac-plasmons in the closely related TI material Bi_2Se_3. One can in any case exclude thermal effects associated to a Bose–Einstein distribution, given that states with ~ 1 eV have a very low occupation probability at room temperatures. Disentangling the specific mechanisms explaining

our observations requires dedicated theoretical simulations mapping the EELS response of Bi_2Te_3 with different structural and geometric configurations and is left for future work.

3. Summary and outlook

In this work we have presented a systematic, spatially-resolved investigation of the energy-gain region of EELS spectral images acquired on Bi_2Te_3 specimens. The main motivation was to avoid the inelastic continuum that pollutes the energy-loss region, which may prevent identifying exotic phenomena appearing at ΔE values below a few eV.
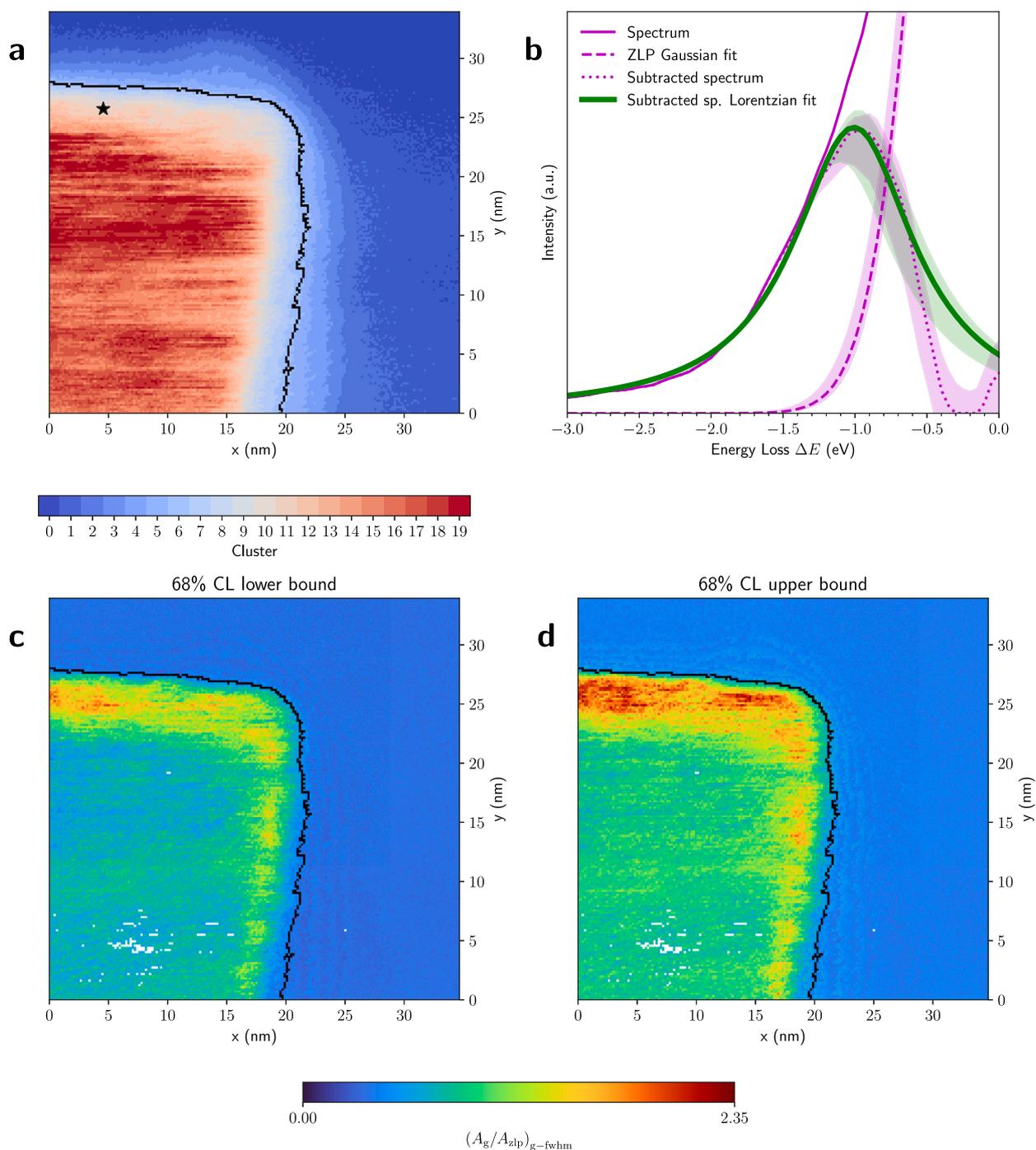
Fig. 4. Energy-gain peak characterisation with the Monte Carlo replica method. **(a)** The EELS spectral image of Fig. 1**c** classified into 20 clusters, each of them composed by pixels with similar thickness. **(b)** Same as Fig. 2**b** now using the Monte Carlo replica method to estimate and propagate the ZLP fitting model uncertainties. For the ZLP Gaussian fit, the subtracted spectrum, and the Lorentzian fit to the latter we display both the median over replicas and the 68% CL intervals. **(c,d)** Same as Fig. 3**c** now the lower and upper ranges, respectively, of the 68% CL interval for the area ratio evaluated over the Monte Carlo replicas. See Fig. S4 in the Supplementary Material for the corresponding median map.

An automated peak-identification procedure identifies a narrow feature located around $\Delta E \sim -0.8$ eV whose intensity and significance are strongly enhanced in regions characterised by sharp thickness variations, such as surfaces and edges. We assess the role of methodological uncertainties associated to e.g. the ZLP subtraction procedure and find that our results are robust against them. The observed resonance could be the signature of edge- and surface-plasmons such as those reported in Bi_2Se_3, thought dedicated simulations would be required to unambiguously ascertain its origin.

While here we focus in Bi_2Te_3 as a proof-of-concept, our approach for ZLP substraction and energy-gain peak tracking is fully general and

can be deployed to any specimen for which EELS-SI measurements are acquired, and in particular it is amenable to atomically thin materials of the van der Waals family. Our approach is made available in the new release of the EELSFITTER framework and hence can be straightforwardly used by other researchers aiming to explore the information contained in the energy-gain region of EELS-SI to identify, model, and correlate localised collective excitations in nanostructured materials. Possible future improvements include the extension to multiple gain-peaks deconvolution and the improved modelling of the loss region describing the inelastic continuum background. All in all, our findings illustrate the powerful reach of energy-gain EELS to accurately map

and characterise the signatures of collective excitations and other exotic resonances arising in quantum materials.

4. Methods

Specimen preparation. The specimen used in this study were Bi_2Te_3 flakes that were mechanically exfoliated from bulk crystals through sonication in isopropanol (IPA) at a ratio of 2 mg of Bi_2Te_3 per 1 ml of IPA. The exfoliated flakes were then transferred onto holey carbon grids for EELS investigations.

STEM-EELS settings. The scanning transmission electron microscopy (STEM) images and electron energy-loss/gain spectra were obtained using a JEOL200F monochromated equipped with aberration corrector and a Gatan Imaging Filter (GIF) continuum spectrometer. The instrument was operated at 200 kV and the convergence semi-angle was 14 mrad. The collection semi-angle for EELS acquisition was 18.3 mrad obtained by inserting a 5 mm EELS entrance aperture. The EELS dispersion was 50 meV per channel.

Data processing and interpretation. The spatially-resolved maps of the energy-gain peaks and the associated peak identification, fitting, and data analysis techniques were performed using the open-source Python package EELSFITTER. All features presented in this work are available in its latest public release together with the accompanying input EELS spectral images via its GITHUB repository.

Declaration of competing interest

The authors declare that they have no known competing financial interests or personal relationships that could have appeared to influence the work reported in this paper.

Data availability

Data will be made available on request

Appendix A. Supplementary data

Supplementary material related to this article can be found online at https://doi.org/10.1016/j.ultramic.2023.113841. The supplementary material of this manuscript provides technical details on the atomic structure characterisation of Bi_2Te_3, the energy-gain peak identification procedure, the uncertainty estimate using the Monte Carlo replica method, and the analysis of the energy-gain peaks in different Bi_2Te_3 specimens.

References

[1] H. Zhang, et al., Topological insulators in Bi2Se3, Bi2Te3 and Sb2Te3 with a single Dirac cone on the surface, Nat. Phys. 5 (2009) 438–442, http://dx.doi.org/10.1038/nphys1270.

[2] Y. Xia, et al., Observation of a large-gap topological-insulator class with a single Dirac cone on the surface, Nat. Phys. 5 (2009) 398–402, http://dx.doi.org/10.1038/nphys1274.

[3] D. Hsieh, et al., Observation of time-reversal-protected single-Dirac-cone topological-insulator states in Bi_2Te_3 and Sb_2Te_3, Phys. Rev. Lett. 103 (2009) 146401, http://dx.doi.org/10.1103/PhysRevLett.103.146401.

[4] A.N. Grigorenko, M. Polini, K.S. Novoselov, Graphene plasmonics, Nat. Photonics 6 (2012) 749–758, http://dx.doi.org/10.1038/nphoton.2012.262.

[5] P. Di Pietro, et al., Observation of Dirac plasmons in a topological insulator, Nature Nanotechnol. 8 (2013) 556–560, http://dx.doi.org/10.1038/nnano.2013.134.

[6] M. Autore, et al., Plasmon–phonon interactions in topological insulator microrings, Adv. Opt. Mater. 3 (2015) 1257–1263, http://dx.doi.org/10.1002/adom.201400513, https://onlinelibrary.wiley.com/doi/pdf/10.1002/adom.201400513.

[7] J. Yin, et al., Plasmonics of topological insulators at optical frequencies, NPG Asia Mater. 9 (2017) e425, http://dx.doi.org/10.1038/am.2017.149.

[8] F. Giorgianni, et al., Strong nonlinear terahertz response induced by dirac surface states in bi2se3 topological insulator, Nature Commun. 7 (2016) 11421, http://dx.doi.org/10.1038/ncomms11421.

[9] M. Zhao, et al., Visible surface plasmon modes in single Bi2Te3 nanoplate, Nano Lett. 15 (2015) 8331–8335, http://dx.doi.org/10.1021/acs.nanolett.5b03966.

[10] T.J. Whitcher, et al., Correlated plasmons in the topological insulator bi2se3 induced by long-range electron correlations, NPG Asia Mater. 12 (2020) 37, http://dx.doi.org/10.1038/s41427-020-0218-7.

[11] A. Kitaev, J. Preskill, Topological entanglement entropy, Phys. Rev. Lett. 96 (2006) 110404, http://dx.doi.org/10.1103/PhysRevLett.96.110404.

[12] L. Fu, C.L. Kane, Superconducting proximity effect and majorana fermions at the surface of a topological insulator, Phys. Rev. Lett. 100 (2008) 096407, http://dx.doi.org/10.1103/PhysRevLett.100.096407.

[13] X. Zhang, J. Wang, S.-C. Zhang, Topological insulators for high-performance terahertz to infrared applications, Phys. Rev. B 82 (2010) 245107, http://dx.doi.org/10.1103/PhysRevB.82.245107.

[14] Y.L. Chen, et al., Experimental realization of a three-dimensional topological insulator, Bi2Te3, Science 325 (2009) 178–181, http://dx.doi.org/10.1126/science.1173034, https://www.science.org/doi/pdf/10.1126/science.1173034.

[15] M.-W. Chu, et al., Probing bright and dark surface-plasmon modes in individual and coupled noble metal nanoparticles using an electron beam, Nano Lett. 9 (2009) 399–404, http://dx.doi.org/10.1021/nl803270x.

[16] F.J. García de Abajo, Optical excitations in electron microscopy, Rev. Modern Phys. 82 (2010) 209–275, http://dx.doi.org/10.1103/RevModPhys.82.209.

[17] V. Myroshnychenko, et al., Plasmon spectroscopy and imaging of individual gold nanodecahedra: A combined optical microscopy, cathodoluminescence, and electron energy-loss spectroscopy study, Nano Lett. 12 (2012) 4172–4180, http://dx.doi.org/10.1021/nl301742h.

[18] T. Coenen, et al., Nanoscale spatial coherent control over the modal excitation of a coupled plasmonic resonator system, Nano Lett. 15 (2015) 7666–7670, http://dx.doi.org/10.1021/acs.nanolett.5b03614.

[19] H.C. Nerl, et al., Probing the local nature of excitons and plasmons in few-layer mos2, npj 2D Mater. Appl. 1 (2017) 2, http://dx.doi.org/10.1038/s41699-017-0003-9.

[20] M.J. Lagos, A. Trügler, U. Hohenester, P.E. Batson, Mapping vibrational surface and bulk modes in a single nanocube, Nature 543 (2017) 529–532, http://dx.doi.org/10.1038/nature21699.

[21] A.B. Yankovich, et al., Visualizing spatial variations of plasmon–exciton polaritons at the nanoscale using electron microscopy, Nano Lett. 19 (2019) 8171–8181, http://dx.doi.org/10.1021/acs.nanolett.9b03534.

[22] O.L. Krivanek, et al., Vibrational spectroscopy in the electron microscope, Nature 514 (2014) 209–212, http://dx.doi.org/10.1038/nature13870.

[23] R. Egoavil, et al., Atomic resolution mapping of phonon excitations in stem-eels experiments, Ultramicroscopy 147 (2014) 1–7, http://dx.doi.org/10.1016/j.ultramic.2014.04.011.

[24] A.A. Govyadinov, et al., Probing low-energy hyperbolic polaritons in van der waals crystals with an electron microscope, Nature Commun. 8 (2017) 95, http://dx.doi.org/10.1038/s41467-017-00056-y.

[25] K. Venkatraman, B.D.A. Levin, K. March, P. Rez, P.A. Crozier, Vibrational spectroscopy at atomic resolution with electron impact scattering, Nat. Phys. 15 (2019) 1237–1241, http://dx.doi.org/10.1038/s41567-019-0675-5.

[26] F.S. Hage, G. Radtke, D.M. Kepaptsoglou, M. Lazzeri, Q.M. Ramasse, Single-atom vibrational spectroscopy in the scanning transmission electron microscope, Science 367 (2020) 1124–1127, http://dx.doi.org/10.1126/science.aba1136.

[27] R. Qi, et al., Four-dimensional vibrational spectroscopy for nanoscale mapping of phonon dispersion in bn nanotubes, Nature Commun. 12 (2021) 1179, http://dx.doi.org/10.1038/s41467-021-21452-5.

[28] A. Brokkelkamp, et al., Spatially resolved band gap and dielectric function in two-dimensional materials from electron energy loss spectroscopy, J. Phys. Chem. A 126 (2022) 1255–1262, http://dx.doi.org/10.1021/acs.jpca.1c09566.

[29] L.I. Roest, S.E. van Heijst, L. Maduro, J. Rojo, S. Conesa-Boj, Charting the low-loss region in electron energy loss spectroscopy with machine learning, Ultramicroscopy 222 (2021) 113202, http://dx.doi.org/10.1016/j.ultramic.2021.113202.

[30] H. Boersch, J. Geiger, W. Stickel, Interaction of 25-kev electrons with lattice vibrations in lif. experimental evidence for surface modes of lattice vibration, Phys. Rev. Lett. 17 (1966) 379–381, http://dx.doi.org/10.1103/PhysRevLett.17.379.

[31] A. Asenjo-Garcia, F.J.G. de Abajo, Plasmon electron energy-gain spectroscopy, New J. Phys. 15 (2013) 103021, http://dx.doi.org/10.1088/1367-2630/15/10/103021.

[32] J.C. Idrobo, et al., Temperature measurement by a nanoscale electron probe using energy gain and loss spectroscopy, Phys. Rev. Lett. 120 (2018) 095901, http://dx.doi.org/10.1103/PhysRevLett.120.095901.

[33] N. Peranio, et al., Low loss eels and eftem study of bi2te3 based bulk and nanomaterials, MRS Online Proc. Libr. (OPL) 1329 (2011) mrss11–1329–i10–21, http://dx.doi.org/10.1557/opl.2011.1238.

[34] V. Nascimento, et al., Xps and eels study of the bismuth selenide, J. Electron Spectrosc. Relat. Phenom. 104 (1999) 99–107, http://dx.doi.org/10.1016/S0368-2048(99)00012-2.

[35] P. Torruella, et al., Assessing oxygen vacancies in bismuth oxide through eels measurements and dft simulations, J. Phys. Chem. C 121 (2017) 24809–24815, http://dx.doi.org/10.1021/acs.jpcc.7b06310.

[36] Y. Li, et al., Plasmonic hot electrons from oxygen vacancies for infrared light-driven catalytic co2 reduction on bi2o3-x, Angew. Chem. Int. Ed. 60 (2021) 910–916, http://dx.doi.org/10.1002/anie.202010156, https://onlinelibrary.wiley.com/doi/pdf/10.1002/anie.202010156.

[37] S.E. van Heijst, et al., Illuminating the electronic properties of ws2 polytypism with electron microscopy, Ann. Phys. 533 (2021) 2000499, http://dx.doi.org/10.1002/andp.202000499, https://onlinelibrary.wiley.com/doi/pdf/10.1002/andp.202000499.

[38] G. Watt, R.S. Thorne, Study of Monte Carlo approach to experimental uncertainty propagation with MSTW 2008 PDFs, J. High Energy Phys. 2012 (2012) 52, http://dx.doi.org/10.1007/JHEP08(2012)052.

[39] The NNPDF Collaboration et al., Neural network determination of parton distributions: the nonsinglet case, J. High Energy Phys. 2007 (2007) 039, http://dx.doi.org/10.1088/1126-6708/2007/03/039.

[40] R.D. Ball, et al., Parton distributions for the LHC Run II, J. High Energy Phys. 04 (2015) 040, http://dx.doi.org/10.1007/JHEP04(2015)040, 1410.8849.

[41] N.P. Hartland, et al., A Monte Carlo global analysis of the Standard Model Effective Field Theory: the top quark sector, J. High Energy Phys. 04 (2019) 100, http://dx.doi.org/10.1007/JHEP04(2019)100, 1901.05965.

[42] A. Candido, et al., Neutrino structure functions from GeV to EeV energies, J. High Energy Phys. 05 (2023) 149, http://dx.doi.org/10.1007/JHEP05(2023)149, 2302.08527.

[43] N. Talebi, et al., Wedge dyakonov waves and dyakonov plasmons in topological insulator bi2se3 probed by electron beams, ACS Nano 10 (2016) 6988–6994, http://dx.doi.org/10.1021/acsnano.6b02968.